J. Fluid Mech. (1986), *vol.* 169, *pp.* 229–250
Printed in Great Britain

Bifurcations in Couette flow between almost corotating cylinders

By M. NAGATA†

School of Mathematics, The University of Newcastle upon Tyne,
Newcastle upon Tyne NE1 7RU, UK

(Received 9 October 1984 and in revised form 5 February 1986)

Transition to turbulence in a circular Couette system is followed numerically up to the state beyond the second bifurcation in the limit of the narrow gap between coaxial cylinders which rotate with almost equal speeds in the same direction. Taylor-vortex flow, which emerges after the Taylor number T exceeds its critical value $T_c = 1708$, becomes unstable to two different types of non-axisymmetric disturbances, depending on $\mathscr{R}$ (the Reynolds number) and Ω, which measure the velocity difference between the cylinders and the mean angular velocity respectively. Finite-amplitude calculations show that one part of the bifurcating flow is characterized by the vortices winding out of phase in the axial direction but still keeping the boundaries between vortices unaffected. The other is distinguished by the vortex dislocation. The inflow as well as the outflow boundaries between vortices are wavy. Both types of solutions are stationary in the frame of reference rotating with the angular velocity Ω.

1. Introduction

The problem of instabilities occurring in flows between rotating coaxial cylinders can be traced back to the early works by Rayleigh (1880) and Taylor (1921, 1923). Since then, because of its simple configuration, the circular Couette system has served as a suitable testing ground for comparison between experimental observations and theories on transition to turbulence. Because the papers written on this system are too numerous and have revealed too complex a variety of transition sequences to mention them all, we refer to just two text books, by Chandrasekhar (1961) and Drazin & Reid (1981), for a general review and the article by DiPrima & Swinney (1981) for its emphasis on dynamical systems. In contrast to the huge amount of work done for the counter-rotating case and the case with the outer cylinder at rest, the only thorough study concentrating on the case with corotating cylinders is the recent work by Andereck, Dickman & Swinney (1983). Using an apparatus with radius ratio 0.883, they found five new types of flow. The reason that there has been less attention given to the corotating case, in spite of its relevance in the astrophysical and geophysical context, seems to partially rest on the fact that mathematically the case is closely related to the convection problem, which has already been explored rigorously. In fact, the axisymmetric Taylor problem of the corotating case in the limit of no curvature effect becomes identical with the two-dimensional problem of convection in the horizontal layer heated from below, with the Prandtl number unity, up to the second bifurcation. However, once the problem depends on the third dimension, a separate treatment is required and at this level of bifurcation, which

† Present address: Department of Applied Mathematics and Theoretical Physics, University of Cambridge, Silver Street, Cambridge CB3 9EW, UK.

lies far beyond the linear criticality, the analysis must resort to numerical calculation. This is the region which the present paper is to investigate. A relatively simple manipulation of the rectangular coordinate system also gives the basis for the analysis on the successive bifurcations to be followed.

2. The formulation of the problem

We consider a viscous incompressible fluid between two concentric cylinders of infinite extent in the axial direction. The inner and the outer cylinders, with radii R_i and R_o respectively, can rotate independently about their common axis with angular velocities Ω_i and Ω_o. The motion (u_r, u_θ, u_ζ) of this fluid is governed by the following equations in a cylindrical coordinate frame (r, θ, ζ) which is uniformly rotating with mean angular velocity $\bar{\Omega} = \frac{1}{2}(\Omega_i + \Omega_o)$:

$$\left.\begin{aligned}
&\frac{\partial u_r}{\partial r} + \frac{u_\theta}{r} + \frac{1}{r}\frac{\partial u_\theta}{\partial \theta} + \frac{\partial u_\zeta}{\partial \zeta} = 0,\\
&\frac{\mathrm{D}u_r}{\mathrm{D}t} - \frac{u_\theta^2}{r} - 2u_\theta\bar{\Omega} = -\frac{\partial p}{\partial r} + \nu\left(\nabla^2 u_r - \frac{u_r}{r^2} - \frac{2}{r^2}\frac{\partial u_\theta}{\partial \theta}\right),\\
&\frac{\mathrm{D}u_\theta}{\mathrm{D}t} + \frac{u_r u_\theta}{r} + 2u_r\bar{\Omega} = -\frac{1}{r}\frac{\partial p}{\partial \theta} + \nu\left(\nabla^2 u_\theta - \frac{u_\theta}{r^2} + \frac{2}{r^2}\frac{\partial u_r}{\partial \theta}\right),\\
&\frac{\mathrm{D}u_\zeta}{\mathrm{D}t} = -\frac{\partial p}{\partial \zeta} + \nu\nabla^2 u_\zeta,
\end{aligned}\right\} \tag{1}$$

where ν is the kinematic viscosity and the pressure p includes all the scalar quantities reducible to gradient terms in the equations. The material derivative

$$\frac{\mathrm{D}}{\mathrm{D}t} = \frac{\partial}{\partial t} + u_r\frac{\partial}{\partial r} + \frac{u_\theta}{r}\frac{\partial}{\partial \theta} + u_\zeta\frac{\partial}{\partial \zeta},$$

and the Laplacian operator

$$\nabla^2 = \frac{1}{r}\frac{\partial}{\partial r}\left(r\frac{\partial}{\partial r}\right) + \frac{1}{r^2}\frac{\partial^2}{\partial \theta^2} + \frac{\partial^2}{\partial \zeta^2},$$

have been employed.

The Couette solution

$$\left.\begin{aligned}
&U_r = 0, \quad U_\theta = -\tfrac{1}{2}(\Omega_i - \Omega_o)\frac{R_o^2 + R_i^2}{R_o^2 - R_i^2}r + (\Omega_i - \Omega_o)\frac{R_o^2 R_i^2}{R_o^2 - R_i^2}\frac{1}{r}, \quad U_\zeta = 0,\\
&\frac{\mathrm{d}P}{\mathrm{d}r} = U_\theta\left(\frac{U_\theta}{r} + 2\bar{\Omega}\right),
\end{aligned}\right\} \tag{2}$$

satisfying the no-slip boundary conditions on both cylinders

$$\left.\begin{aligned}
&r = R_i; \quad u_r = 0, \quad u_\theta = \tfrac{1}{2}(\Omega_i - \Omega_o)R_i, \quad u_\zeta = 0,\\
&r = R_o; \quad u_r = 0, \quad u_\theta = -\tfrac{1}{2}(\Omega_i - \Omega_o)R_o, \quad u_\zeta = 0,
\end{aligned}\right\} \tag{3}$$

is known to exhibit the simplest symmetry that takes place in the real situation. We deal with the transition sequence bifurcating from this basic state.

In order to simplify the problem, we assume that the gap $D = R_o - R_i$ between the cylinders is sufficiently small compared with the mean radius $\bar{R} = \frac{1}{2}(R_i + R_o)$,

$$D \ll \bar{R}.$$

Further, the angular velocity of a fluid with respect to the rotating frame of reference is assumed to be much smaller than $\bar{\Omega}$,

$$\frac{u_\theta}{\bar{R}} \ll \bar{\Omega}.$$

Since it is reasonable to suppose that

$$O(u_r) \sim O(u_\theta)$$

in general, the use of the rectangular coordinate system

$$x = \frac{(r-\bar{R})}{D}, \quad y = \frac{\bar{R}\theta}{D}, \quad z = \frac{\zeta}{D},$$

can be assured. Taking D^2/ν as the timescale, ν/D as the velocity scale and ν^2/D^2 as the pressure scale, we get the non-dimensionalized equations for fluctuations $\boldsymbol{u} = (u, v, w)$ and p from the basic state

$$U = 0, \quad V = -\mathscr{R}x, \quad W = 0; \tag{4}$$

$$\boldsymbol{\nabla}\cdot\boldsymbol{u} = 0 \tag{5a}$$

$$\frac{\partial \boldsymbol{u}}{\partial t} + \boldsymbol{u}\cdot\boldsymbol{\nabla}\boldsymbol{u} + V\frac{\partial}{\partial y}\boldsymbol{u} + u\frac{\mathrm{d}V}{\mathrm{d}x}\hat{\boldsymbol{j}} + \Omega\hat{\boldsymbol{k}}\times\boldsymbol{u} = -\boldsymbol{\nabla}p + \nabla^2\boldsymbol{u}, \tag{5b}$$

where the unit vectors $\hat{\boldsymbol{j}}$ and $\hat{\boldsymbol{k}}$ correspond to the y- and z-directions respectively (see figure 1), and the operators $\boldsymbol{\nabla}$ and ∇^2 take the Cartesian expressions. Thus, the subsequent bifurcations are determined by two parameters:

$$\mathscr{R} = \frac{(\Omega_\mathrm{i}-\Omega_\mathrm{o})\,\bar{R}D}{\nu} \quad \text{the Reynolds number} \tag{6}$$

and

$$\Omega = \frac{(\Omega_\mathrm{i}+\Omega_\mathrm{o})\,D^2}{\nu}. \tag{7}$$

The strength of the shear across the cylinders is represented by $\mathscr{R}$ whereas Ω measures the Coriolis effect.

It is convenient to separate the fluctuation $\boldsymbol{u}$ into the average part

$$\hat{\boldsymbol{j}}\check{V}(t, x) = \bar{\boldsymbol{u}} \tag{8}$$

and the residual

$$\check{\boldsymbol{u}}(t, x, y, z) = \boldsymbol{u} - \hat{\boldsymbol{j}}\check{V}. \tag{9}$$

The average, indicated by the bar, is taken in the y- and z directions. Therefore, the mean velocity field $\hat{V}$, which is the yz-average of the total flow, is modified by $\check{V}$ from the basic state V:

$$\hat{V}(t, x) = V(x) + \check{V}(t, x). \tag{10}$$

Then, we introduce the general expression for the solenoidal vector field $\check{\boldsymbol{u}}$ in terms of poloidal and toroidal parts

$$\check{\boldsymbol{u}} = \boldsymbol{\nabla}\times(\boldsymbol{\nabla}\times\hat{\boldsymbol{\imath}}\phi) + \boldsymbol{\nabla}\times\hat{\boldsymbol{\imath}}\psi, \tag{11}$$

where $\hat{\boldsymbol{\imath}}$ is the unit vector in the x-direction and ϕ and ψ are scalar functions with

$$\bar{\phi} = \bar{\psi} = 0. \tag{12}$$

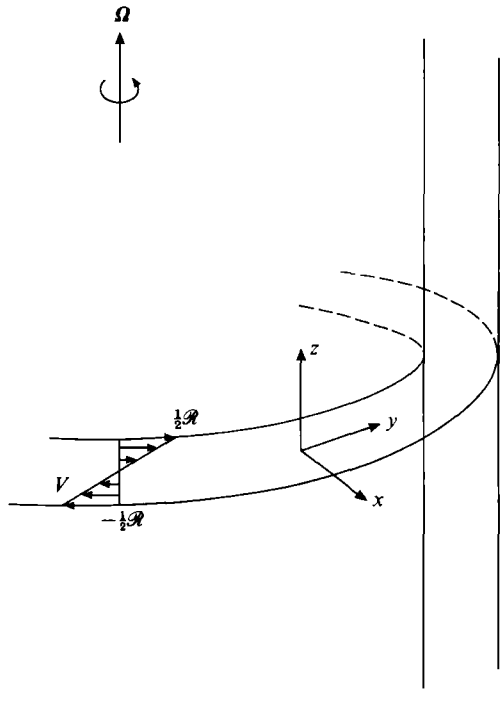

FIGURE 1. Configuration of the model. The analysis deals with the narrow-gap limit without curvature effect.

Operations $\hat{\boldsymbol{i}}\cdot\boldsymbol{\nabla}\times\boldsymbol{\nabla}\times$ and $\hat{\boldsymbol{i}}\cdot\boldsymbol{\nabla}\times$ on (5*b*) lead to

$$\nabla^4 \Delta_2 \phi = \Omega \partial_z \Delta_2 \psi + \hat{V} \partial_y \nabla^2 \Delta_2 \phi - \frac{\partial^2 \hat{V}}{\partial x^2} \partial_y \Delta_2 \phi + \hat{\boldsymbol{i}}\cdot\boldsymbol{\nabla}\times\boldsymbol{\nabla}\times[\check{\boldsymbol{u}}\cdot\boldsymbol{\nabla}\check{\boldsymbol{u}}] + \frac{\partial}{\partial t}\nabla^2 \Delta_2 \phi, \quad (13a)$$

$$\nabla^2 \Delta_2 \psi = -\Omega \partial_z \Delta_2 \phi + \hat{V} \partial_y \Delta_2 \psi - \frac{\partial \hat{V}}{\partial x} \partial_z \Delta_2 \phi - \hat{\boldsymbol{i}}\cdot\boldsymbol{\nabla}\times[\check{\boldsymbol{u}}\cdot\boldsymbol{\nabla}\check{\boldsymbol{u}}] + \frac{\partial}{\partial t}\Delta_2 \psi, \quad (13b)$$

where $\Delta_2 = (\partial^2/\partial y^2) + (\partial^2/\partial z^2)$.

Further, by taking the yz-average of the y-component of (5*b*), we obtain the expression for the modification of the mean velocity by the action of the Reynolds stress:

$$\frac{\partial \check{V}}{\partial t} - \frac{\partial^2 \check{V}}{\partial x^2} = \frac{\partial}{\partial x} \overline{\Delta_2 \phi (\partial_{xy}^2 \phi + \partial_z \psi)}.$$

Prescribed no-slip conditions on the boundaries are

$$\phi = \frac{\partial \psi}{\partial x} = \psi = \check{V} = 0 \quad \text{at } x = \pm\tfrac{1}{2}. \quad (14)$$

3. The Taylor vortex

Experiments suggest that for the narrow-gap case Couette flow becomes unstable with respect to steady axisymmetric disturbances when the Taylor number T, defined in (19), exceeds some critical value T_c provided $\mu = \Omega_o/\Omega_i$ is less than one. In our system

$$\mu = \frac{\Omega_o}{\Omega_i} = \frac{\Omega - (D/\bar{R})\mathscr{R}}{\Omega + (D/\bar{R})\mathscr{R}}$$

and without loss of generality we can take only the positive values of Ω. Therefore, we expect that the Taylor-vortex solution bifurcates first for $\mathscr{R} > 0$ when T exceeds T_c.

Letting $\partial/\partial t$ and $\partial/\partial y$ in (13) be zero we get

$$(\partial_{xx}^2+\partial_{zz}^2)^2\,\partial_{zz}^2\phi-\Omega\partial_{zzz}^3\psi = \partial_{xz}^2[(\partial_{xz}^2\phi\partial_z-\partial_{zz}^2\phi\partial_x)\,\partial_{xz}^2\phi] + \partial_{zz}^2[(\partial_{xz}^2\phi\partial_z-\partial_{zz}^2\phi\partial_x)\,\partial_{zz}^2\phi], \tag{16a}$$

$$(\partial_{xx}^2+\partial_{zz}^2)\,\partial_{zz}^2\psi+\left(\Omega+\frac{\mathrm{d}\check{V}}{\mathrm{d}x}\right)\partial_{zzz}^3\phi = \partial_z(\partial_{xz}^2\phi\partial_z-\partial_{zz}^2\phi\partial_x)\,\partial_z\psi], \tag{16b}$$

$$\frac{\mathrm{d}^2\check{V}}{\mathrm{d}x^2} = -\frac{\mathrm{d}}{\mathrm{d}x}\overline{(\partial_{zz}^2\phi\,\partial_z\psi)}, \tag{16c}$$

with the boundary conditions (14)

$$\phi = \frac{\partial\phi}{\partial x} = \psi = \check{V} = 0 \quad \text{at } x = \pm\tfrac{1}{2}. \tag{17}$$

It is noteworthy that the above equations and the boundary conditions can be reduced to those of the two-dimensional problem of convection in a horizontal layer ($-\frac{1}{2} \leqslant x \leqslant \frac{1}{2}$) heated from below with a Prandtl number of 1. In fact, substitutions of

$$\Theta = \Omega(\partial_z\psi+\check{V}) \tag{18}$$

and

$$T = \Omega(\mathscr{R}-\Omega), \tag{19}$$

and simple manipulations on (16), lead to

$$(\partial_{xx}^2+\partial_{zz}^2)^2\,\partial_{zz}^2\phi-\partial_{zz}^2\Theta = \partial_{xz}^2[(\partial_{xz}^2\phi\partial_z-\partial_{zz}^2\phi\partial_x)\,\partial_{xz}^2\phi] + \partial_{zz}^2[(\partial_{xz}^2\phi\partial_z-\partial_{zz}^2\phi\partial_x)\,\partial_{zz}^2\phi], \tag{20a}$$

$$(\partial_{xx}^2+\partial_{zz}^2)\,\Theta-T\partial_{zz}^2\phi = \partial_{xz}^2\phi\partial_z\Theta-\partial_{zz}^2\phi\partial_x\Theta, \tag{20b}$$

where Θ and $-\partial_{zz}^2\phi$ represent the temperature deviation from the conductive state and the vertical component of velocity respectively, with the boundary conditions

$$\phi = \frac{\partial\phi}{\partial x} = \Theta = 0 \quad \text{at } x = \pm\tfrac{1}{2}. \tag{21}$$

In this context, T defines the Rayleigh number. It is well known from the nonlinear theory of convection (Clever & Busse 1974) that the two-dimensional roll solution with horizontal wavenumber $\gamma = 3.117$ sets in supercritically when the Rayleigh number is increased above its critical value of 1708.

The analysis starts with finding finite-amplitude Taylor-vortex solutions numerically above the $T = \Omega(\mathscr{R}-\Omega) = 1708$ curve in the $(\Omega, \mathscr{R})$-space whose first quadrant is bounded by the rigid rotation line $\mathscr{R} = 0$ and the plane-Couette-flow limit $\Omega = 0$ (see figure 2). The Taylor number is positive or negative in the regions above or below the Rayleigh line $\mathscr{R} = \Omega$ ($T = 0$) and for each curve of $T = \text{const.}$ (> 0) the minimum values of $\mathscr{R}$ occur on the line $\Omega = \frac{1}{2}\mathscr{R}$.

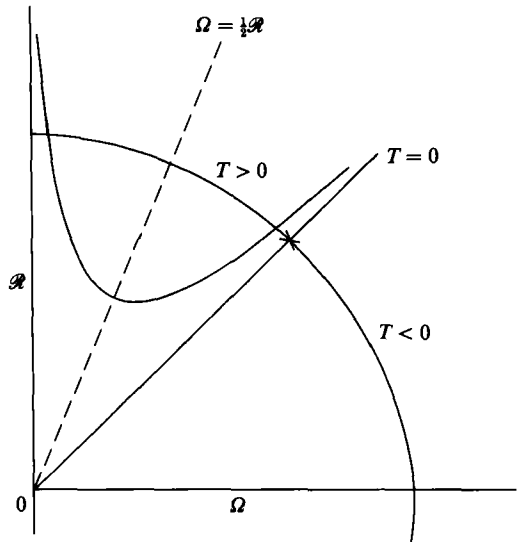

FIGURE 2. The Taylor number $T = \Omega(\mathscr{R} - \Omega)$.

After ϕ, ψ and $\check{V}$ are expanded by sets of orthogonal functions in each direction so that (12) and (17) are satisfied, i.e. (see Chandrasekhar 1961)

$$\phi = \sum_{l=1}^{\infty} \sum_{n=-\infty}^{\infty} a_{ln} \, \mathrm{e}^{\mathrm{i}n\gamma z} f_l(x), \tag{22a}$$

$$\psi = \sum_{l=1}^{\infty} \sum_{n=-\infty}^{\infty} b_{ln} \, \mathrm{e}^{\mathrm{i}n\gamma z} g_l(x), \tag{22b}$$

$$\check{V} = \sum_{k=1}^{\infty} c_k \sin 2k\pi x, \tag{22c}$$

where

$$f_l(x) = \begin{cases} \dfrac{\cosh \nu_{\frac{1}{2}(l+1)} x}{\cosh \frac{1}{2}\nu_{\frac{1}{2}(l+1)}} - \dfrac{\cos \nu_{\frac{1}{2}(l+1)} x}{\cos \frac{1}{2}\nu_{\frac{1}{2}(l+1)}} & (l: \text{odd}), \\ \dfrac{\sinh \mu_{\frac{1}{2}l} x}{\sinh \frac{1}{2}\mu_{\frac{1}{2}l}} - \dfrac{\sin \mu_{\frac{1}{2}l} x}{\sin \frac{1}{2}\mu_l} & (l: \text{even}), \end{cases} \tag{23a}$$

$$g_l(x) = \sin l\pi(x + \tfrac{1}{2}) \tag{23b}$$

and ν_i, μ_i are solutions of

$$\tanh \tfrac{1}{2}\nu_i - \tanh \tfrac{1}{2}\nu_i = 0, \tag{24a}$$

$$\coth \tfrac{1}{2}\mu_i - \cot \tfrac{1}{2}\mu_i = 0, \tag{24b}$$

we multiply $\mathrm{e}^{-\mathrm{i}n'\gamma z} f_{l'}(x)$, $\mathrm{e}^{-\mathrm{i}n'\gamma z} g_{l'}(x)$ and $\sin 2k'\pi x$ by (16a, b, c) respectively, and take the average in the x- and z-directions.

For numerical purposes, the resulting infinite set of nonlinear homogeneous algebraic equations for expansion coefficients a_{ln}, b_{ln} and c_k must be truncated. Omitting coefficients and equations which do not satisfy

$$l + |n| \leqslant N_{\mathrm{T}}, \quad k \leqslant N'_{\mathrm{T}}, \tag{25}$$

where the truncation parameters N_{T} and N'_{T} are some integers (usually $N'_{\mathrm{T}} \approx \frac{1}{2}N_{\mathrm{T}}$ since $f_l(x)$ or $g_l(x)$ includes both symmetric and antisymmetric functions whereas

$\sin 2k\pi x$ is antisymmetric in x), we use the Newton–Raphson method in which initially guessed values for q_i, representing a_{ln}, b_{ln}, and c_k, are iterated until they scarcely change as the iteration number I_t is increased by one:

$$\left|\frac{q_i^{(I_t+1)}-q_i^{(I_t)}}{q_i^{(I_t)}}\right|<\epsilon \quad (i=1,2,\ldots). \tag{26}$$

We choose $\epsilon = 1.0\times 10^{-5}$.

The total number of q_i can be reduced by three quarters for fixed truncation numbers compared with all the possible combinations of integers l and n if the symmetric properties of ϕ and ψ are taken into account. First, since ϕ and ψ are real,

$$a_{l-n}=a_{ln}^*, \quad b_{l-n}=b_{ln}^*,$$

where the asterisk denotes the complex-conjugate. Secondly, interacting components are limited to the case where $l+n$ = even,

$$a_{l-n}=a_{ln}, \quad b_{l-n}=-b_{ln},$$

because of the properties of nonlinear terms in the equations and the fact that $\hat{V}$ is antisymmetric in x. In trigonometric notation, the set $\mathscr{U}_0$ of closed interacting components

$$\mathscr{U}_0=\begin{Bmatrix} \phi: & \cos n^{+}\gamma z & F_{\mathrm{s}}(x) \\ & \cos n^{++}\gamma z & F_{\mathrm{a}}(x) \\ \psi: & \sin n^{+}\gamma z & F_{\mathrm{s}}(x) \\ & \sin n^{++}\gamma z & F_{\mathrm{a}}(x) \end{Bmatrix} \tag{27}$$

is to be considered where n^+ and n^{++} denote odd and even integers respectively, and $F_{\mathrm{s}}(x)$ and $F_{\mathrm{a}}(x)$ represent symmetric and antisymmetric functions in x.

Following Nagata & Busse (1983), well-converged values of coefficients of lower harmonics are compared for different truncation parameters. It is found that $N_{\mathrm{T}}=6$ or 8 is sufficient depending on $T<2500$ or $T<25600$. Even for $T\approx 250000$, $N_{\mathrm{T}}=10$ is good enough for reasonable accuracy; only 56 coefficients are included in the latter truncation level.

Figure 3 shows a part of the region where Taylor-vortex solutions are obtained. The finite-amplitude vortices appear supercritically except for the wavenumber γ less than 1.4. In the region between $\gamma\approx 1.4$ and the neutral stability curve values of coefficients did not converge showing random oscillations, without correlation among themselves, with respect to iterations. However, outside the neutral curve, disturbances became smaller and smaller by iterations retrieving to the Couette-flow solution.

Lines of constant values of the stream function $\partial\phi/\partial z$ on the meridional plane are shown in figure 4 for the typical Taylor number. Since the critical Taylor number occurs at the wavenumber $\gamma=3.117$, the most unstable bifurcating vortex is confined to a torus of almost square cross-section ($\pi/\gamma\approx 1$). As the Taylor number is increased, the circulation of the vortices becomes stronger keeping the centre of each vortex unchanged in position. In addition to the circulations with alternating sense along the vertical direction, the velocity field consists of the horizontal disturbance component $\partial\psi/\partial z$ whose profiles on the middle plane $x=0$ are depicted in figure 5 for various values of T. In view of the convection problem, ϕ and $\Theta=\Omega(\partial_z\psi+\hat{V})$ are determined by $T(=T(\mathscr{R},\Omega))$ only. Therefore, the strength of the circulation is invariant with fixed value of T whereas the vertical shear gets stronger as Ω decreases.

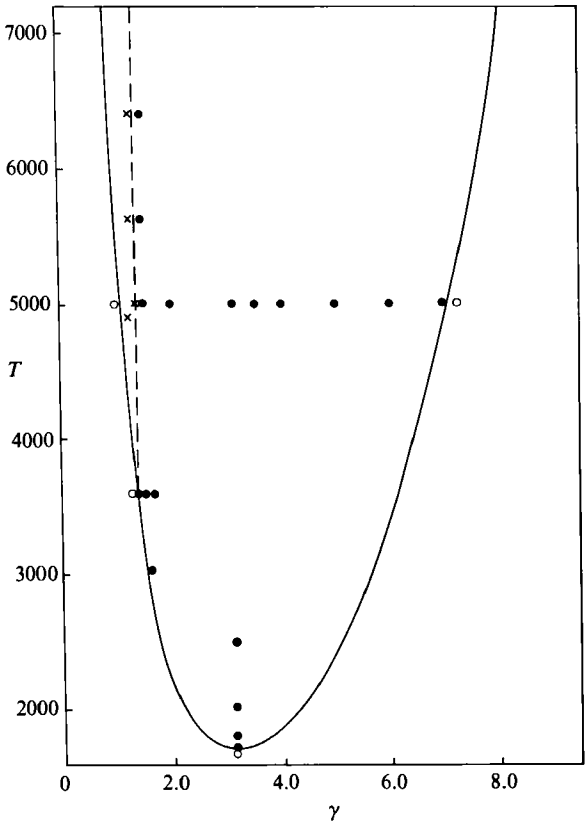

FIGURE 3. The Taylor number T as a function of the wavenumber γ according to linear theory (solid line): ●, parameter values for which the nonlinear Taylor-vortex solutions have been obtained; ○, points where the circular-Couette-flow solutions are retrieved; ×, indicates when attempts to obtain a converged solution failed.

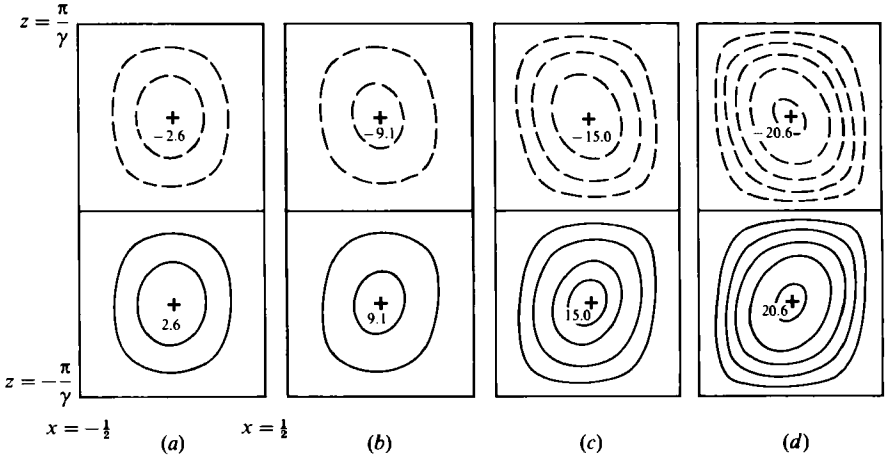

FIGURE 4. Lines of constant values of the stream function $\partial\phi/\partial z$ on the meridional plane for different values of T. $\Omega = \frac{1}{2}\mathscr{R}$, $\gamma = 3.117$. (*a*) $T = 2500$, $\Delta = 1.0$; (*b*) $T = 10000$, $\Delta = 4.0$; (*c*) $T = 22500$, $\Delta = 4.0$; (*d*) $T = 40000$, $\Delta = 4.0$.

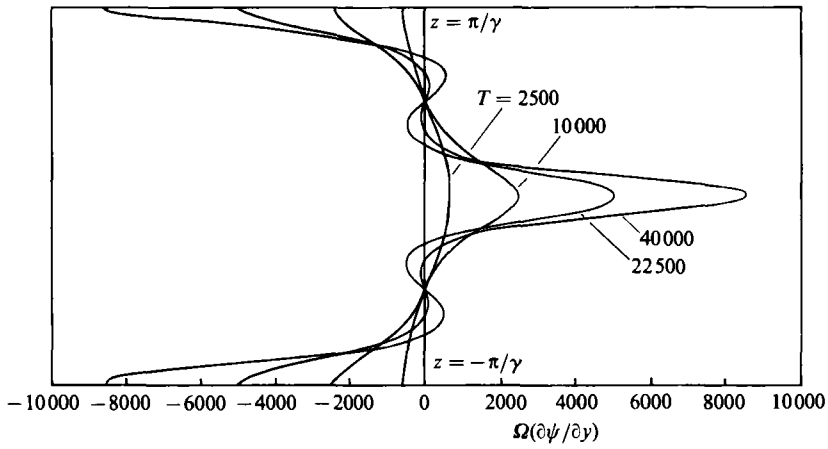

FIGURE 5. The profile of the horizontal component $\partial\psi/\partial z$ of the disturbance velocity $\breve{u}$ for different values of T. $\gamma = 3.117$.

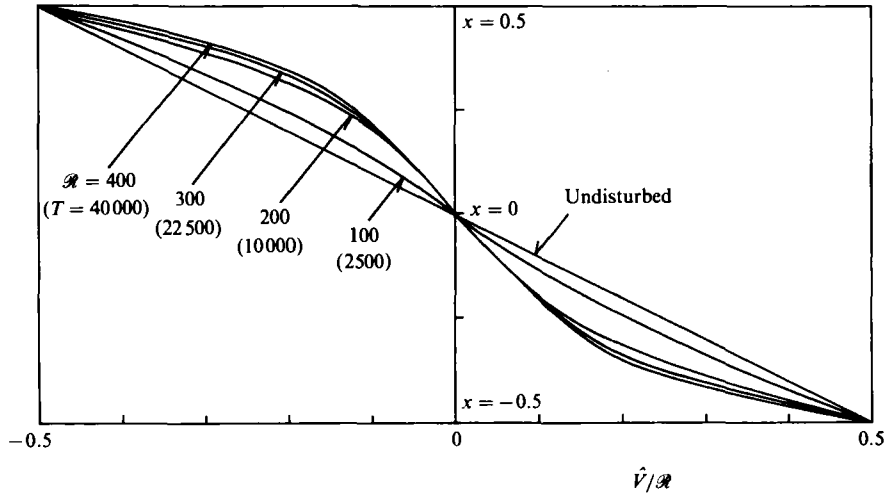

FIGURE 6. The modification of the mean flow $\hat{V} = V + \breve{V}$ for different values of T. $\Omega = \frac{1}{2}\mathscr{R}$, $\gamma = 3.117$.

In the plane-Couette-flow limit ($\Omega \to 0$), $\partial\psi/\partial z$ approaches infinity on the vortex boundaries for each $T \geqslant 1708$. The jet-stream structure near the vortex boundaries and additional inflexion points for large T seem to be responsible for instabilities of axisymmetric vortex flows especially when Ω is relatively small. Figure 6 shows how the mean flow $\hat{V} = V + \breve{V}$ is modified as $\mathscr{R}$ increases. It appears that the modification becomes saturated for $\mathscr{R}$ greater than 400. It is appropriate to use torque, the value of $-\mathrm{d}\hat{V}/\mathrm{d}x$ at $x = \pm\frac{1}{2}$, as the measure of the strength of the Taylor vortex. As shown in figure 7, the wavenumber at which the strongest torque is exerted is in the central range, which is shifted from 3.117 to a larger value with increasing Taylor numbers. Correspondingly, the mean flow $\hat{V} = V + \breve{V}$ is less modified towards smaller or larger values of γ for which finite-amplitude solutions are possible (figure 8), indicating that the momentum transport is not effective for vortices with wavenumber γ outside the central range.

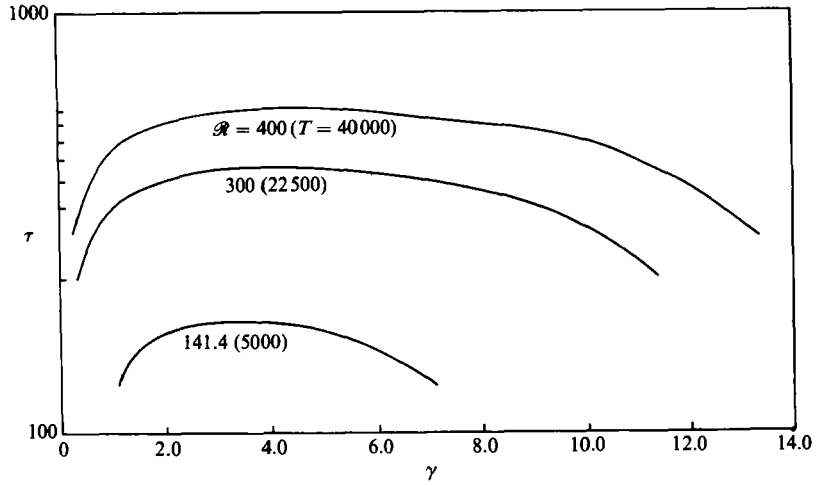

FIGURE 7. The torque $\tau = -\mathrm{d}\hat{V}/\mathrm{d}x|_{x=\pm\frac{1}{2}}$ exerted by the Taylor vortices on the walls as a function of the wavenumber γ for different values of T. $\Omega = \frac{1}{2}\mathscr{R}$.

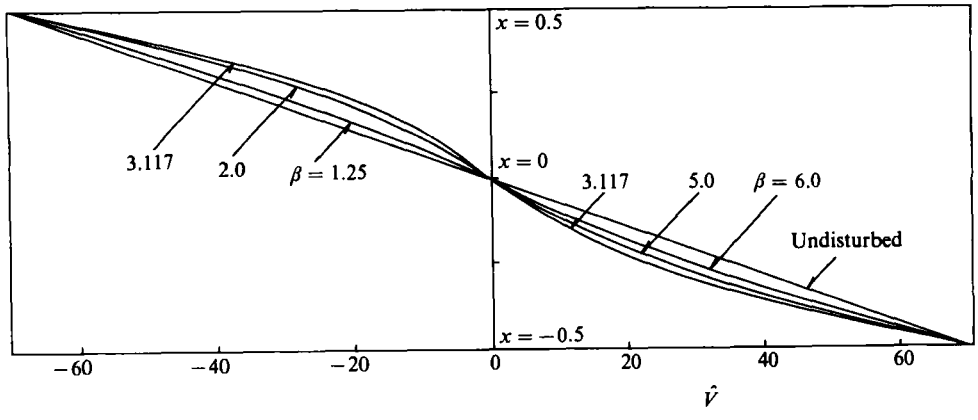

FIGURE 8. The modification of the mean flow $\hat{V}$ for different values of γ. $T = 5000$, $\Omega = \frac{1}{2}\mathscr{R}$. β is the azimuthal wavenumber.

4. Stability of the Taylor vortex

In order to examine the stability of axisymmetric Taylor vortices, we superimpose an arbitrary three-dimensional infinitesimal perturbation

$$\tilde{\boldsymbol{u}} = \{\boldsymbol{\nabla} \times (\boldsymbol{\nabla} \times \hat{\boldsymbol{i}}\tilde{\phi}) + \boldsymbol{\nabla} \times \hat{\boldsymbol{i}}\tilde{\psi}\} \tag{28}$$

on steady finite-amplitude solutions $\boldsymbol{u}$. Neglecting quadratic terms in (13a, b), we get

$$\left(\hat{V}\partial_y - \left(\nabla^2 - \frac{\partial}{\partial t}\right)\right)\nabla^2 \Delta_2 \tilde{\phi} - \frac{\partial^2 \hat{V}}{\mathrm{d}x^2}\partial_y \Delta_2 \tilde{\phi} + \Omega \partial_z \Delta_2 \tilde{\psi} + \hat{\boldsymbol{i}} \cdot \boldsymbol{\nabla} \times \boldsymbol{\nabla} \times [\tilde{\boldsymbol{u}} \cdot \boldsymbol{\nabla}\check{\boldsymbol{u}} + \check{\boldsymbol{u}} \cdot \boldsymbol{\nabla}\tilde{\boldsymbol{u}}] = 0, \tag{29a}$$

$$\left(\hat{V}\partial_y - \left(\nabla^2 - \frac{\partial}{\partial t}\right)\right)\Delta_2 \psi - \left(\frac{\mathrm{d}\hat{V}}{\mathrm{d}x} + \Omega\right)\partial_z \Delta_2 \tilde{\phi} - \tilde{\boldsymbol{i}} \cdot \boldsymbol{\nabla} \times [\tilde{\boldsymbol{u}} \cdot \boldsymbol{\nabla}\check{\boldsymbol{u}} + \check{\boldsymbol{u}} \cdot \boldsymbol{\nabla}\tilde{\boldsymbol{u}}] = 0. \tag{29b}$$

Since the steady solution $\boldsymbol{u}$ is periodic in z, infinitesimal perturbations have the same periodicity as $\boldsymbol{u}$ with additional exponential dependencies in the y- and z-directions as well as time t:

$$\tilde{\phi} = \sum_{l=1}^{\infty} \sum_{n=-\infty}^{\infty} \tilde{a}_{ln}\, \mathrm{e}^{\mathrm{i}n\gamma z} f_l(x)\, \mathrm{e}^{\mathrm{i}(dy+bz)+\sigma t}, \tag{30a}$$

$$\tilde{\psi} = \sum_{l=1}^{\infty} \sum_{n=-\infty}^{\infty} \tilde{b}_{ln}\, \mathrm{e}^{\mathrm{i}n\gamma z} g_l(x)\, \mathrm{e}^{\mathrm{i}(dy+bz)+\sigma t}. \tag{30b}$$

The growth rate σ is to be evaluated for each Floquet parameter d and b, which are taken to be positive real. By multiplying (29a) and (29b) by $\mathrm{e}^{-\mathrm{i}n'\gamma z} f_{l'}(x)$ and $\mathrm{e}^{-\mathrm{i}n'\gamma z} g_{l'}(x)$, and taking the average in the x- and z-directions, (29) can be reduced to the eigenvalue problem

$$\boldsymbol{F}\boldsymbol{X} = \sigma \boldsymbol{X}. \tag{31}$$

The matrix $\boldsymbol{F}$ is not symmetric in general and the eigenvector $\boldsymbol{X}$ is composed of coefficients $\tilde{a}_{ln}$, $\tilde{b}_{ln}$ with l, n satisfying (25) at the same truncation level as the steady axisymmetric vortices $\boldsymbol{u}$. We regard the steady axisymmetric vortices as stable provided that all the eigenvalues σ have negative real parts. On the other hand, the flow is regarded as unstable if there exists at least one eigenvalue whose real part is positive. In contrast to the steady finite-amplitude axisymmetric solutions, $\tilde{\phi}$ and $\tilde{\psi}$ are complex. Also the coefficients $\tilde{a}_{ln}$, $\tilde{b}_{ln}$ with $n = 0$ are allowed (the components with $n = 0$ are taken care of by $\hat{V}$ in the steady axisymmetric solutions). The first terms in (29a) and (29b) show that $\tilde{\phi}$ and $\tilde{\psi}$ lose their symmetric properties in x because $\hat{V}$ is antisymmetric in x. Furthermore, terms including Ω in the coefficients indicate that the symmetric properties in z are also lost when $b \neq 0$, because of the partial derivative of z. The above argument allows us to concentrate on two different sets of interacting components $\tilde{\boldsymbol{u}}_{\mathrm{I}}$ and $\tilde{\boldsymbol{u}}_{\mathrm{II}}$ when $b = 0$:

$$\tilde{\boldsymbol{u}}_{\mathrm{I}} = \left\{ \begin{array}{l} \tilde{\phi}: \left\{ \begin{array}{l} \cos n^{++}\gamma z \left\{ \begin{array}{l} F_{\mathrm{s}}(x) \\ F_{\mathrm{a}}(x) \end{array} \right. \\ \cos n^{+}\gamma z \left\{ \begin{array}{l} F_{\mathrm{s}}(x) \\ F_{\mathrm{a}}(x) \end{array} \right. \end{array} \right. \\ \tilde{\psi}: \left\{ \begin{array}{l} \sin n^{++}\gamma z \left\{ \begin{array}{l} F_{\mathrm{s}}(x) \\ F_{\mathrm{a}}(x) \end{array} \right. \\ \sin n^{+}\gamma z \left\{ \begin{array}{l} F_{\mathrm{a}}(x) \\ F_{\mathrm{s}}(x) \end{array} \right. \end{array} \right. \end{array} \right\}, \tag{32a}$$

$$\tilde{\boldsymbol{u}}_{\mathrm{II}} = \left\{ \begin{array}{l} \tilde{\phi}: \left\{ \begin{array}{l} \sin n^{++}\gamma z \left\{ \begin{array}{l} F_{\mathrm{a}}(x) \\ F_{\mathrm{s}}(x) \end{array} \right. \\ \sin n^{+}\gamma z \left\{ \begin{array}{l} F_{\mathrm{a}}(x) \\ F_{\mathrm{s}}(x) \end{array} \right. \end{array} \right. \\ \tilde{\psi}: \left\{ \begin{array}{l} \cos n^{++}\gamma z \left\{ \begin{array}{l} F_{\mathrm{a}}(x) \\ F_{\mathrm{s}}(x) \end{array} \right. \\ \cos n^{+}\gamma z \left\{ \begin{array}{l} F_{\mathrm{a}}(x) \\ F_{\mathrm{s}}(x) \end{array} \right. \end{array} \right. \end{array} \right\}. \tag{32b}$$

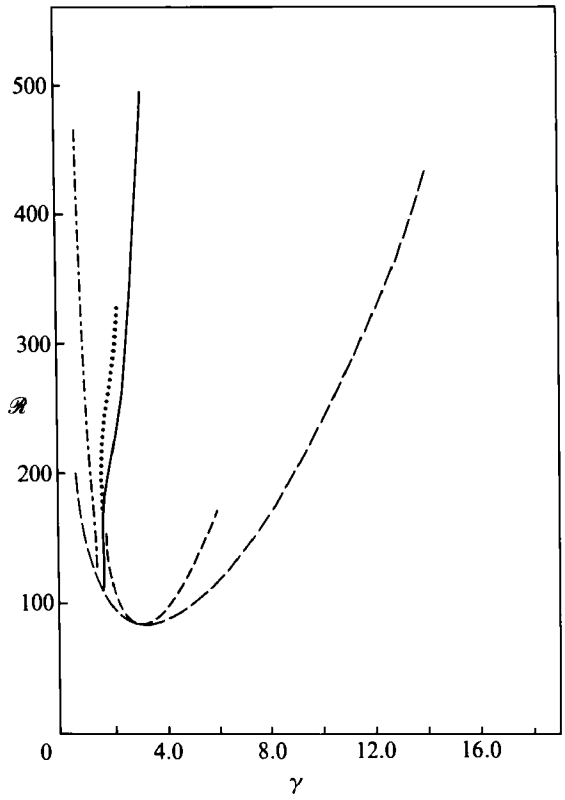

FIGURE 9. Stability regime of the Taylor vortices for $\Omega = \frac{1}{2}\mathscr{R}$. The outer parabolic curve (– – –) indicates results of linear theory. The region of stable Taylor vortices is bounded by the sideband instability boundary (- - - -) from below and the in-phase mode instability (——) from the left. The boundary of onset of the out-of-phase mode instability (·····) is also shown. Steady solutions could not be obtained in the region to the left of the line (·—·—·—).

The notations n^+, n^{++}, F_a, F_s are described following (27). For $b \neq 0$ components from $\tilde{\mathscr{U}}_I$ and from $\tilde{\mathscr{U}}_{II}$ interact each other, creating the combined set $\tilde{\mathscr{U}}_{I+II}$:

$$\tilde{\mathscr{U}}_{I+II} = \tilde{\mathscr{U}}_I + \tilde{\mathscr{U}}_{II}. \tag{33}$$

Since $\tilde{\boldsymbol{u}}_z = \partial_{zx}^2 \tilde{\phi} - \partial_y \tilde{\psi}$, vortices are confined by the horizontal planes of zero vertical velocity for the set $\tilde{\mathscr{U}}_I$, in contrast to the case $\tilde{\mathscr{U}}_{II}$ where boundaries between vortices are wavy.

For the majority of the calculations we choose 10 for the truncation number N_T, in which case the rank of the matrix $\boldsymbol{F}$ becomes 200 for $b \neq 0$. The growth rate at the truncation level $N_T = 10$ differs by only 1 % from the value at $N_T = 9$ when $\mathscr{R} = 200$ and $\Omega = 100$. However, the convergence gets worse as $\mathscr{R}$ increases. For example, when $\mathscr{R} = 450$ and $\Omega = 225$ it is 15 % at $N_T = 10$. Since the stability analysis serves to provide some guidance for pursuing nonlinear analysis for non-axisymmetric vortices, which will be described in the next section, the relatively rough evaluation will be permissible.

In figure 9 the axisymmetric vortices are shown to be stable for $\Omega = \frac{1}{2}\mathscr{R}$ in the region bounded by the sideband instability boundary from below and by the in-phase mode instability boundary from left. The sideband instability is characterized by axisymmetric modulation ($d = 0$) and therefore its occurrence is identical with that

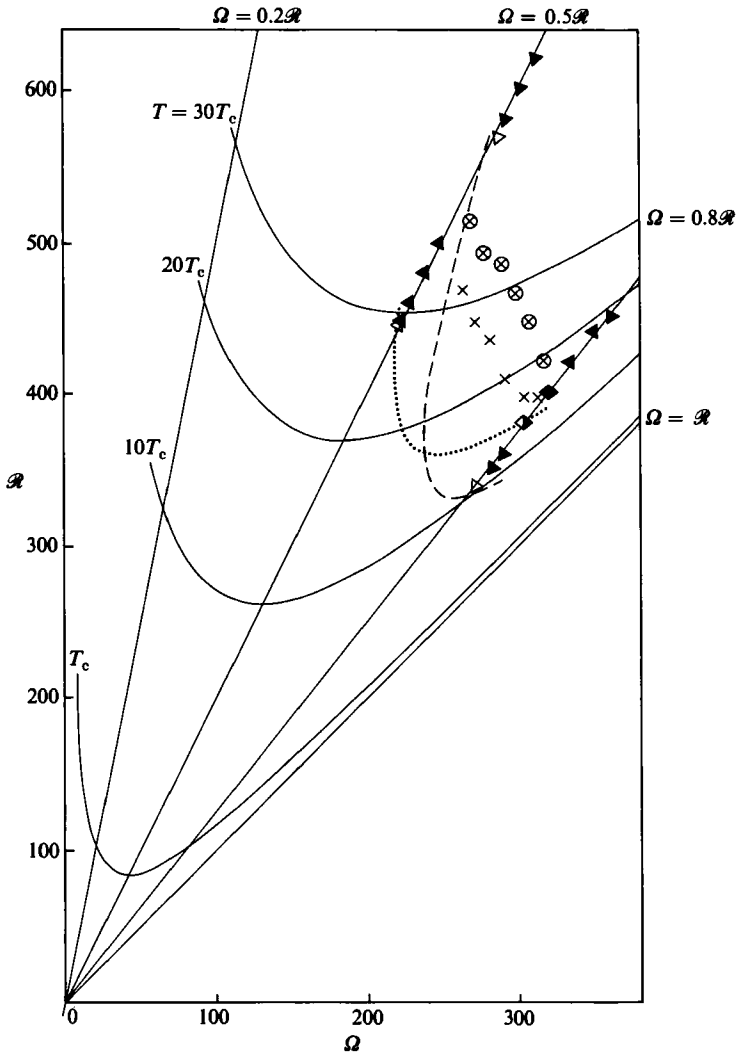

FIGURE 10. Points in $(\Omega, \mathscr{R})$-space where non-axisymmetric solutions were detected; $\gamma = 3.117$: ▲, class $\mathscr{A}_1$, $\beta = 3.8$ on $\Omega = 0.5\,\mathscr{R}$, $\beta = 4.0$ on $\Omega = 0.8\,\mathscr{R}$; ▲, class $\mathscr{A}_2$, $\beta = 4.5$ on $\Omega = 0.5\,\mathscr{R}$, $\beta = 2.2$ on $\Omega = 0.8\,\mathscr{R}$. The stability boundaries of the Taylor vortex-flow against the in-phase mode (dotted line) as well as the out-of-phase mode (dashed line) are estimated by the stability analysis. △, points where the Taylor-vortex solutions are retrieved by decreasing $\mathscr{R}$ along the lines of $\Omega/\mathscr{R} = \text{const}$; × and ⊗, the onset of the twisted Taylor vortices and the wavy-inflow-boundary vortices with twists, respectively, observed by Andereck *et al.* (1983).

of the convection problem (Clever & Busse 1974). It grows monotonously, showing common features which can be seen in other contexts; i.e. the maximum growth rate resides on $b/\gamma = \frac{1}{4}$ or $\frac{3}{4}$ (Nagata & Busse 1983). The in-phase mode instability results from interaction of the disturbance component in the set $\tilde{\mathscr{U}}_{\mathrm{I}}$ and occurs at $b = 0$. Also shown in figure 9 is the out-of-phase mode instability which occurs at $b = 0$ as well. The set $\tilde{\mathscr{U}}_{\mathrm{II}}$ is responsible for this. The calculations in the case of $\Omega = 0.8\mathscr{R}$ reveals that the out-of-phase mode instability becomes dominant rather than the in-phase mode instability. The preferred values of d for the onset of each mode decrease as

$\Omega/\mathscr{R}$ increases. For instance, $d = 3.8$ on $\Omega = 0.5\mathscr{R}$ and $d = 3.1$ on $\Omega = 0.8\mathscr{R}$ for $\tilde{\mathscr{U}}_{\mathrm{I}}$, whereas $d = 4.3$ on $\Omega = 0.5\mathscr{R}$ and $d = 2.2$ on $\Omega = 0.8\mathscr{R}$ for $\tilde{\mathscr{U}}_{\mathrm{II}}$ when $\gamma = 3.117$. Both the in-phase and the out-of-phase mode instabilities grow monotonously.

Although it is not shown in figure 9, instabilities showing an oscillatory mode ($\mathrm{Im}\,[\sigma] \neq 0$) have been detected at $b \approx \frac{1}{2}\gamma$ and $d \approx 2$ for the set $\tilde{\mathscr{U}}_{\mathrm{I+II}}$. For instance, when $\mathscr{R} = 250$, $\Omega = 0.5\mathscr{R}$, $b = \frac{1}{2}\gamma$ and $d = 2$, the growth rate with the biggest real part is $\sigma = (4.0 \pm 0.3\mathrm{i})$ at $\gamma = 1.5$ and $\sigma = (19.3 \pm 1.6\mathrm{i})$ at $\gamma = 1.2$. The in-phase mode and the out-of-phase mode at $b = 0$ have the real growth rates $\sigma = 5.2$ and $\sigma = 2.5$ respectively, when $\gamma = 1.5$. They are 20.6 and 16.7 when $\gamma = 1.2$ with $d = 2$. The fact that this subharmonic oscillatory mode becomes as dominant as the monotonously growing modes when the wavenumber γ gets smaller seems to be related to the inability to obtain well-converged axisymmetric solutions above the neutral curve for $\gamma \lesssim 1.4$ described in §3, although the Newton–Raphson iteration method does not necessarily follow the exact timesteps.

5. Non-axisymmetric finite-amplitude vortices

The fact that the steady axisymmetric vortices become unstable with respect to monotonously growing instabilities in the class $\tilde{\mathscr{U}}_{\mathrm{I}}$ or $\tilde{\mathscr{U}}_{\mathrm{II}}$ depending on Ω is encouraging for seeking steady (in the rotating frame) three-dimensional nonlinear solutions. Also the appropriate values of the wavenumbers γ in the axial direction as well as β in the azimuthal direction can be inferred from the Floquet parameters b and d that have given the maximum growth rate. The wavenumber γ remains the same as for the steady axisymmetric vortices since $b = 0$ for both instabilities resulting from the classes $\tilde{\mathscr{U}}_{\mathrm{I}}$ and $\tilde{\mathscr{U}}_{\mathrm{II}}$, whereas the wavenumber β is set equal to d. Thus the representations assumed for ϕ and ψ are

$$\phi = \sum_{l=1}^{\infty} \sum_{m=-\infty}^{\infty} \sum_{n=-\infty}^{\infty} a_{lmn}\, \mathrm{e}^{\mathrm{i}(m\beta y + n\gamma z)} f_l(x), \tag{34a}$$

$$\psi = \sum_{l=1}^{\infty} \sum_{m=-\infty}^{\infty} \sum_{n=-\infty}^{\infty} b_{lmn}\, \mathrm{e}^{\mathrm{i}(m\beta y + n\gamma z)} g_l(x), \tag{34b}$$

which must satisfy (13a, b) with the time derivative omitted, and the boundary condition (13c).

Since it is found that the simplest set $\mathscr{A}_0$ of three-dimensionally interacting components of ϕ and ψ

$$\mathscr{A}_0 = \left\{ \begin{array}{ll} \phi: & \left\{ \begin{array}{l} \cos m^{+}\beta y \cos n^{+}\gamma z\, F_{\mathrm{s}}(x) \\ \cos m^{++}\beta y \cos n^{++}\gamma z\, F_{\mathrm{a}}(x) \\ \sin m^{+}\beta y \cos n^{+}\gamma z\, F_{\mathrm{a}}(x) \\ \sin m^{++}\beta y \cos n^{++}\gamma z\, F_{\mathrm{s}}(x) \end{array} \right. \\ \psi: & \left\{ \begin{array}{l} \cos m^{+}\beta y \sin n^{+}\gamma z\, F_{\mathrm{s}}(x) \\ \cos m^{++}\beta y \sin n^{++}\gamma z\, F_{\mathrm{a}}(x) \\ \sin m^{+}\beta y \sin n^{+}\gamma z\, F_{\mathrm{a}}(x) \\ \sin m^{++}\beta y \sin n^{++}\gamma z\, F_{\mathrm{s}}(x) \end{array} \right. \end{array} \right\} \tag{35}$$

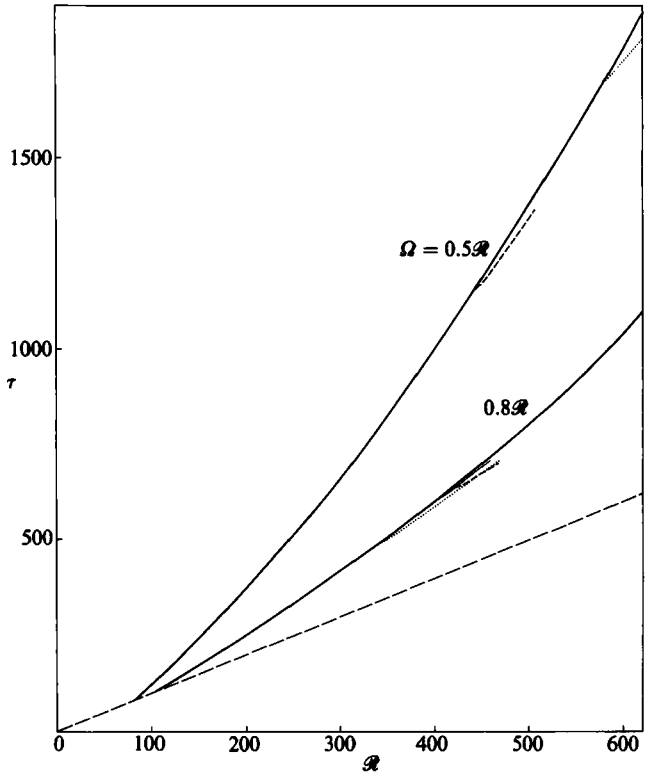

FIGURE 11. The torque as a function of $\mathscr{R}$ for different values of $\Omega/\mathscr{R} = \text{const}$: $\gamma = 3.117$. The Taylor-vortex solutions (——) bifurcate from the circular Couette flow (– – –). The torque is reduced as the onset of non-axisymmetric solutions (----, the class $\mathscr{A}_1$ with $\beta = 2.4$; ....., the class $\mathscr{A}_2$ with $\beta = 3.0$). The torque for $\mathscr{A}_1$ with $\beta = 3.8$ is shown (——) on $\Omega = 0.8\mathscr{R}$.

does not include all the components in $\mathscr{U}_0$, we must seek the possible bifurcation in the next-simplest sets of interacting components (see the Appendix). Among seven such sets, only $\mathscr{A}_1$, $\mathscr{A}_2$, $\mathscr{A}_6$ and $\mathscr{A}_7$ include the set $\mathscr{U}_0$ (choosing $m^{++} = 0$). Furthermore, the sets $\mathscr{A}_6$ and $\mathscr{A}_7$ can be eliminated from the consideration because the stability analysis on $\mathscr{U}_0$ has detected no monotonously growing subharmonic instabilities. Choosing $m^+ = 1$ and setting $\beta = d$, we find that the sets $\mathscr{A}_1$ and $\mathscr{A}_2$ also include all the infinitesimal perturbation components in $\tilde{\mathscr{U}}_{\mathrm{I}}$ and $\tilde{\mathscr{U}}_{\mathrm{II}}$ respectively. Therefore, we expect two different types of three-dimensional solutions to bifurcate from the axisymmetric vortex solutions in terms of the sets $\mathscr{A}_1$ and $\mathscr{A}_2$.

Following the procedure described in §3 (with additional manipulation in the azimuthal direction y), we obtain the non-axisymmetric vortex solutions in the set $\mathscr{A}_1$ as well as $\mathscr{A}_2$. Each type of three-dimensional solution is detected in the $(\Omega, \mathscr{R})$-space as shown in figure 10, where the truncation number $N_{\mathrm{T}} = 10$ has been used in the formula

$$l + 2|m| + |n| \leqslant N_{\mathrm{T}}. \tag{36}$$

This formula has the advantage of reducing drastically the total number of components included in the calculation without greatly affecting convergence because of the strong background components with $m = 0$. Calculations show that the axisymmetric vortex solutions are retained with all the coefficients a_{lmn}, b_{lmn},

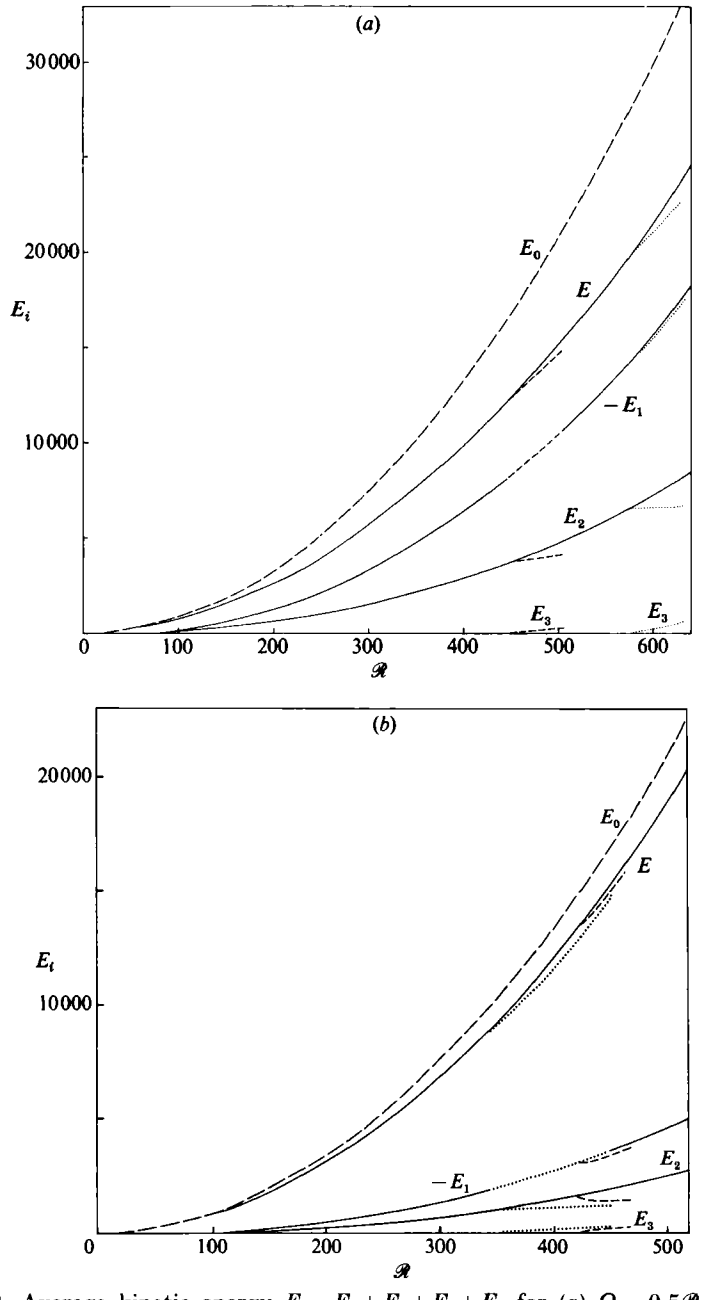

FIGURE 12. Average kinetic energy $E = E_0 + E_1 + E_2 + E_3$ for (*a*) $\Omega = 0.5\mathscr{R}$ and (*b*) $\Omega = 0.8\mathscr{R}$. $E_i (i = 0, 1, 2, 3)$ are defined in equation (38), $\gamma = 3.117$. See the caption of figure 11 for β on each bifurcating curve.

with $m \neq 0$, converging to zero when $\mathscr{R}$ is decreased across the stability limit determined by the linear analysis on the axisymmetric vortices. After the onset of the second bifurcation the torque is found to decrease for both classes as shown in figure 11. The reduced torque required for non-axisymmetric motions has been reported by Eagles (1974), who analysed nonlinear interactions of velocity components up to the cubic order in the case of the outer cylinder at rest.

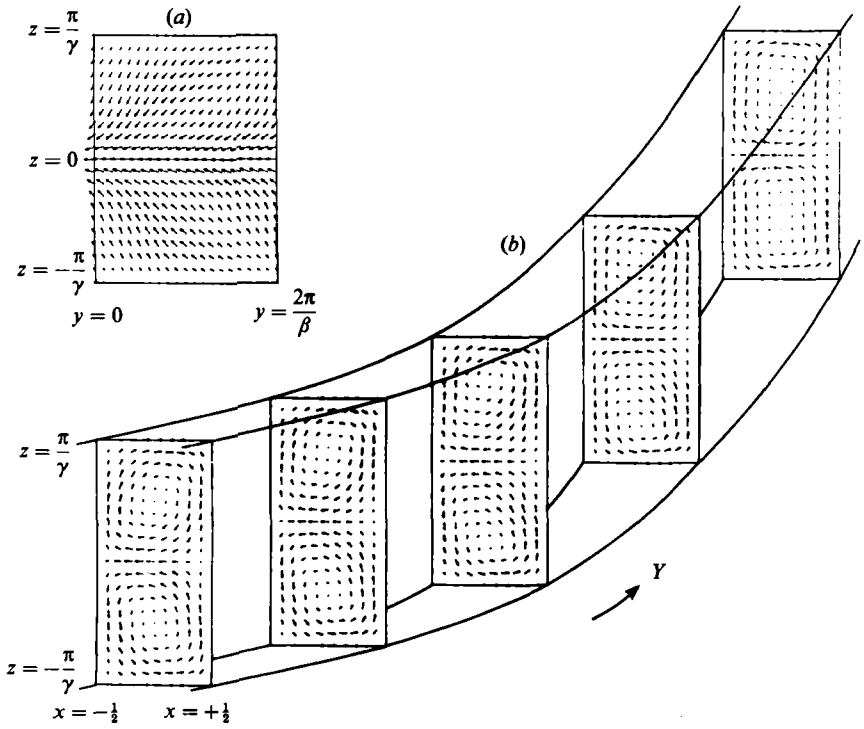

FIGURE 13. The projection of the velocity vector for the non-axisymmetric solution associated with the class $\mathscr{A}_1$ on the planes of (*a*) $x = 0.25$ and (*b*) $y = n\pi/4\beta$ ($n = 0, 1, 2, 3, 4$): $\mathscr{R} = 500$, $\Omega = \frac{1}{2}\mathscr{R}$, $\beta = 4.0$, $\gamma = 3.117$.

The average kinetic energy

$$\begin{aligned}\langle \boldsymbol{u}\cdot\boldsymbol{u}\rangle &= \langle((V+\check{V})\hat{\boldsymbol{j}}+\check{\boldsymbol{u}})\cdot((V+\check{V})\hat{\boldsymbol{j}}+\check{\boldsymbol{u}})\rangle \\ &= \langle(V+\check{V})\rangle + \langle\check{\boldsymbol{u}}\cdot\check{\boldsymbol{u}}\rangle\end{aligned}$$

is calculated for various velocity components:

$$E_0 = \langle V^2\rangle = \tfrac{1}{12}\mathscr{R}, \tag{38a}$$

$$E_1 = \langle(V+\check{V})^2\rangle - \langle V^2\rangle, \tag{38b}$$

$$E_2 = \langle\check{\boldsymbol{u}}\cdot\check{\boldsymbol{u}}\rangle_{m=0}, \tag{38c}$$

$$= \langle|\phi\nabla^2\Delta_2\phi - \psi\Delta_2\psi|\rangle_{m=0},$$

$$E_3 = \langle\check{\boldsymbol{u}}\cdot\check{\boldsymbol{u}}\rangle_{m\neq 0}, \tag{38d}$$

$$= \langle|\phi\nabla^2\Delta_2\phi - \psi\Delta_2\psi|\rangle_{m\neq 0},$$

where the brackets denote the average through the whole volume.

It is apparent from figure 12 that the energy E_3, required for the non-axisymmetric motion, is transferred from the energy E_2 of the axisymmetric parts of the fluctuating motion, while the energy E_1, extracted from the Couette solution V, is almost unchanged, i.e. the energy E_0+E_1 for the mean motion $V+\check{V}$ is nearly the same as for the axisymmetric solution.

In order to visualize the flow pattern the velocity vectors are projected in figures 13 and 14 on the plane $x = 0.25$ as well as the set of meridional planes for both classes.

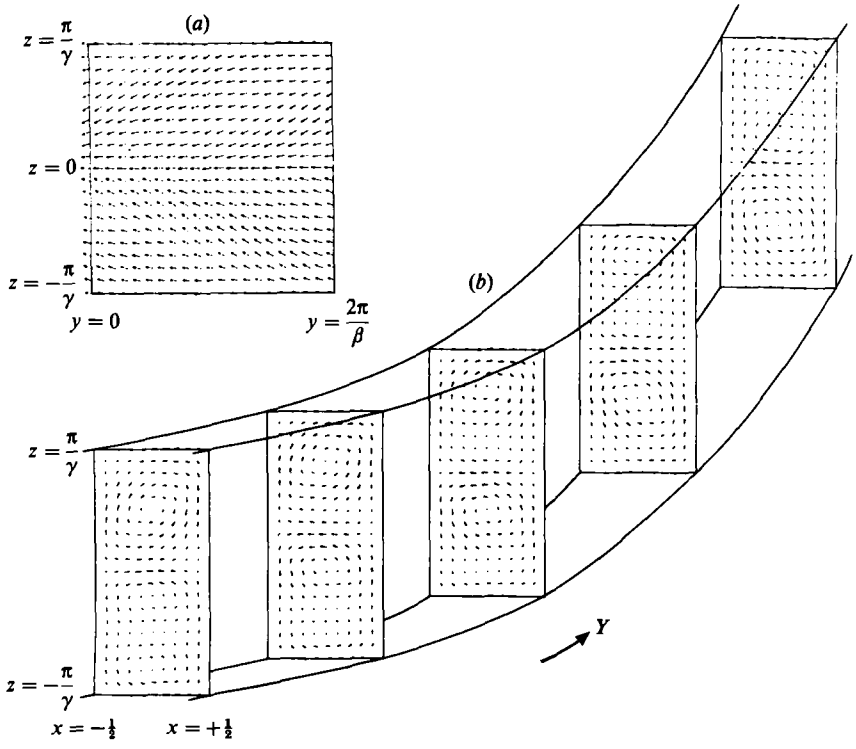

FIGURE 14. The projection of the velocity vector for the non-axisymmetric solution associated with the class $\mathscr{A}_2$ on the planes of (*a*) = 0.25 and (*b*) $y = n\pi/4\beta$ ($n = 0, 1, 2, 3, 4$): $\mathscr{R} = 600$, $\Omega = \frac{1}{5}\mathscr{R}$, $\beta = 3.0, \gamma = 3.117$.

For the class $\mathscr{A}_1$ the centres of the neighbouring vortices are separated and come back alternatively in periodic fashion along the azimuthal direction, keeping the planes of vortex boundaries horizontal. In the class $\mathscr{A}_2$ a new small vortex, which is produced in one cell, becomes as strong as the original vortex along the azimuthal direction. Until the produced vortex becomes weak again and is completely absorbed, the vortex in the neighbouring cell remains almost unchanged. Then the latter vortex follows the same branch-off process as the vortex in the adjacent cell has undertaken. Slight deviations from the horizontal planes are noticeable on the vortex cell boundaries.

6. Concluding remarks

By taking a special limit where the curvature does not play a role in the analysis, the symmetry with respect to the median plane $x = 0$ is established. The reason for the time independency, at least up to the third bifurcation, is attributed to this and we are able to avoid the complicated interaction between wave components propagating with different phase velocities. The observation that the phase velocity approaches the mean velocity of the two concentric cylinders when the radius gap ratio becomes small is reported for other circular Couette systems with the outer cylinder at rest (Jones 1981).

It is interesting to compare the results with the experimental observations by Andereck *et al.* (1983). Of particular interest are the twisted Taylor vortices observed in the region close to the Rayleigh-stability boundary. This flow is characterized by

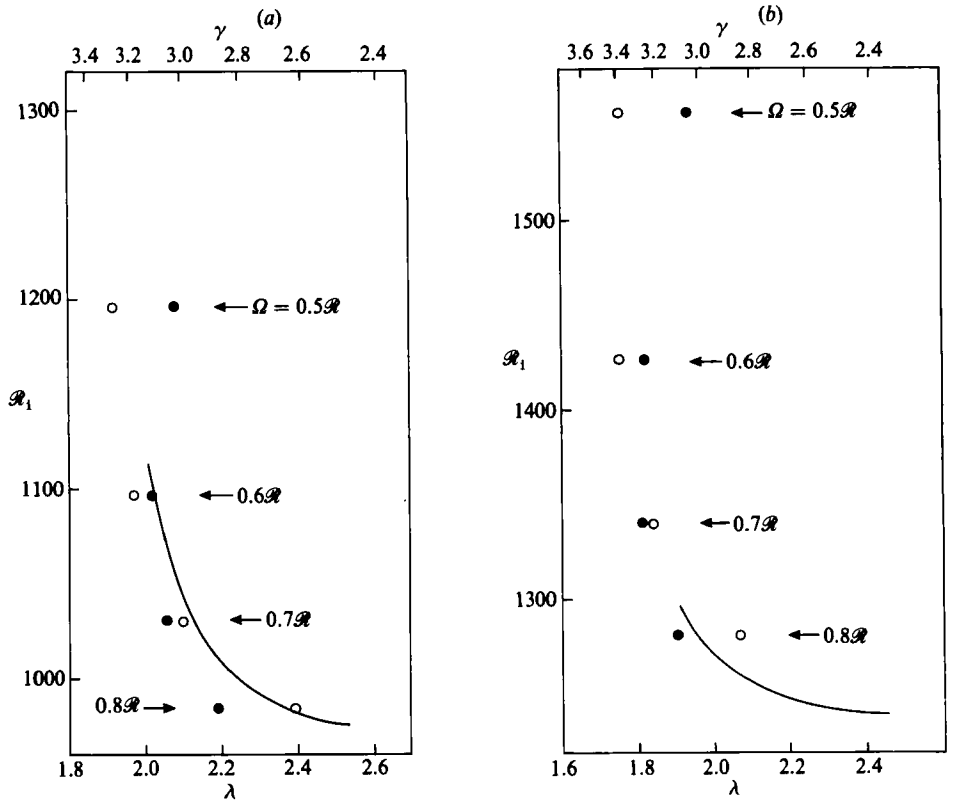

FIGURE 15. Dependence of the inner Reynolds number $\mathscr{R}_1$ for the onset of the twists on the axial wavelength λ of the Taylor vortices by Andereck *et al.* (1983); (*a*) $\mathscr{R}_0 = 815$; (*b*) $\mathscr{R}_0 = 1060$. Open circles and dots indicate the onset of the in-phase mode and the out-of-phase mode respectively, for $\Omega/\mathscr{R} = 0.5$, 0.6, 0.7 and 0.8 obtained by the stability analysis in §4.

a rope-like structure embedded in the Taylor vortices whose boundaries are essentially unaffected by the appearance of the twists. The pattern is in-phase in the axial direction and rotates with the mean angular speed of the cylinders. The inner- and outer-cylinder Reynolds numbers $\mathscr{R}_1$ and $\mathscr{R}_0$ defined by Andereck *et al.* can be expressed in terms of our $\mathscr{R}$ and Ω as follows:

$$\mathscr{R}_1 = \tfrac{1}{2}q\left(\frac{\Omega}{1-q}+\frac{2\mathscr{R}}{1+q}\right), \tag{39a}$$

$$\mathscr{R}_0 = \frac{1}{2}\left(\frac{\Omega}{1-q}-\frac{2\mathscr{R}}{1+q}\right), \tag{39b}$$

where q is the radius ratio of the cylinders. Five sets of data in the $(\mathscr{R}_1, \mathscr{R}_0)$-plane for the occurrence of the twists for $\gamma = \pi$, available from their figure 3, are plotted in the $(\mathscr{R}, \Omega)$-plane for $\gamma = 3.117$ by using (39) with $q = 0.883$ and $\Omega = 0.5\mathscr{R}$ (see figure 10). Andereck *et al.* reported a larger axial wavelength at lower $\mathscr{R}_1$ for the onset of the twists. Their figure 6 is reproduced as figure 15, which also shows the wavenumbers γ for the onset of the in-phase and the out-of-phase modes obtained in the stability analysis for $\Omega/\mathscr{R} = 0.5$, 0.6, 0.7 and 0.8, and plotted against $\mathscr{R}_1$ using (39*a*, *b*). The in-phase mode follows the same tendency as the experimental findings for the twists, whereas the non-dimensional axial wavelength λ becomes smaller at

first and then gets larger as $\mathscr{R}_1$ is decreased for the out-of-phase mode. From these comparisons with the experimental observations the non-axisymmetric flow resulting from the nonlinear interaction of the components in the class $\mathscr{A}_1$ appears to correspond to the twisted Taylor vortices. We found that the azimuthal wavenumber β of the in-phase mode was $\beta = 3.8$ for $\Omega = 0.5\mathscr{R}$ and $\beta = 3.1$ for $\Omega = 0.8\mathscr{R}$. Since the number of twists in each Taylor vortex m ranges from 14 to 16 in the experiments with $\gamma = 2\pi/2.4 = 5\pi/6$, the observed wavenumber β is about half as small as our β if $D/\bar{R} = 0.117/0.91415 = 0.124$ is taken in the expression

$$\beta = mD/\bar{R}. \tag{40}$$

However, it should be noted that the calculations of the torque for $\Omega = 0.8\mathscr{R}$ show that $\beta = 2.4$ instead of 3.1 is most preferred at least for $\mathscr{R} > 420$. Discrepancies seem to result from the curvature effect, which has been neglected ($q = 1$) in the analysis.

It could be conjectured that if the curvature effect were taken into account the crossover point at $(\Omega, \mathscr{R}) \approx (240, 360)$ on $\Omega = \frac{2}{3}\mathscr{R}$ in figure 10 would approach to (320,400) on $\Omega = 0.8\mathscr{R}$, where the onsets of two types of flows, the twists and the wavy-inflow-boundary vortices with twists, seem to coincide experimentally. Then the class $\mathscr{A}_1$ would lose stability at higher $\mathscr{R}$ in the presence of a growing out-of-phase mode for $\Omega < 0.8\mathscr{R}$, just as the experiment exhibits the transition from the twists to the wavy-inflow-boundary vortices with twists. The latter flow has a subharmonic character along the axial direction. Therefore, the experimental counterpart for the class $\mathscr{A}_2$ is not obvious. There might exist another new flow which would correspond to this class for $\Omega > 0.8\mathscr{R}$.

It should also be remembered that only the bifurcation routes through the steady axisymmetric Taylor-vortex solutions have been considered in this paper; that is we have ignored the possibility of direct three-dimensional bifurcations from the circular Couette flow, which might be taking the form of the interacting components in the set $\mathscr{A}_0$ or more entangled sets such as $\mathscr{A}_1+\mathscr{A}_3+\mathscr{A}_7$, $\mathscr{A}_2+\mathscr{A}_4+\mathscr{A}_7$, etc., even in the steady case.

We have seen in the previous section that the onset of the two different classes of steady non-axisymmetric vortex solutions occur in close proximity. In particular, there is a crossover somewhere around $\Omega = \frac{2}{3}\mathscr{R}$ depending on which of the two classes bifurcates first. Therefore it is expected that neither of the classes is as stable when $\mathscr{R}$ is increased beyond the second critical value along the lines of $\mathscr{R}/\Omega = \text{const}$. Although the analysis on the stability of the non-axisymmetric vortex solutions has been formulated and programmed for a bigger computer, calculations have not yet been performed. Since the symmetric properties for interacting components are totally destroyed when $d \neq 0$, the high cost of computations is inevitable even if the truncation formula (36) is applied.

The author would like to thank Professor P. H. Roberts for giving him an opportunity to work under a grant from the Science and Engineering Research Council. Discussions with Professor F. H. Busse and Dr C. A. Jones are gratefully acknowledged. This work was suggested by Professor F. H. Busse and initiated in collaboration with him at UCLA with partial support from the Atmospheric Science Section of NSF.

Appendix

We list the sets of interacting components of ϕ and ψ which satisfy the three-dimensional nonlinear equations. All the following seven sets $\mathscr{A}_i (i = 1, 2, \ldots, 7)$ include $\mathscr{A}_0$ (35) which is also closed for three-dimensional interaction. However, the set $\mathscr{A}_0$ alone does not include the set $\mathscr{U}_0(27)$, which constitutes axisymmetric Taylor vortices.

$$\mathscr{A}_i \supset \mathscr{A}_0 \quad (i = 1, 2, \ldots, 7)$$

$$\mathscr{A}_0 \not\supset \mathscr{U}_0$$

$$\mathscr{A}_1 = \mathscr{A}_0 + \left\{ \phi: \begin{pmatrix} \cos m^{+}\beta y \cos n^{++}\gamma z\, F_a(x) \\ \cos m^{++}\beta y \cos n^{+}\gamma z\, F_s(x) \\ \sin m^{+}\beta y \cos n^{++}\gamma z\, F_s(x) \\ \sin m^{++}\beta y \cos n^{+}\gamma z\, F_a(x) \end{pmatrix} \quad \psi: \begin{pmatrix} \cos m^{+}\beta y \sin n^{++}\gamma z\, F_a(x) \\ \cos m^{++}\beta y \sin n^{+}\gamma z\, F_s(x) \\ \sin m^{+}\beta y \sin n^{++}\gamma z\, F_s(x) \\ \sin m^{++}\beta y \sin n^{+}\gamma z\, F_a(x) \end{pmatrix} \right\}$$

$$\mathscr{A}_2 = \mathscr{A}_0 + \left\{ \phi: \begin{pmatrix} \cos m^{+}\beta y \sin n^{++}\gamma z\, F_a(x) \\ \cos m^{++}\beta y \sin n^{+}\gamma z\, F_s(x) \\ \sin m^{+}\beta y \sin n^{++}\gamma z\, F_s(x) \\ \sin m^{++}\beta y \sin n^{+}\gamma z\, F_a(x) \end{pmatrix} \quad \psi: \begin{pmatrix} \cos m^{+}\beta y \cos n^{++}\gamma z\, F_a(x) \\ \cos m^{++}\beta y \cos n^{+}\gamma z\, F_s(x) \\ \sin m^{+}\beta y \cos n^{++}\gamma z\, F_s(x) \\ \sin m^{++}\beta y \cos n^{+}\gamma z\, F_a(x) \end{pmatrix} \right\}$$

$$\mathscr{A}_3 = \mathscr{A}_0 + \left\{ \phi: \begin{pmatrix} \cos m^{+}\beta y \cos n^{++}\gamma z\, F_s(x) \\ \cos m^{++}\beta y \cos n^{+}\gamma z\, F_a(x) \\ \sin m^{+}\beta y \cos n^{++}\gamma z\, F_a(x) \\ \sin m^{++}\beta y \cos n^{+}\gamma z\, F_s(x) \end{pmatrix} \quad \psi: \begin{pmatrix} \cos m^{+}\beta y \sin n^{++}\gamma z\, F_s(x) \\ \cos m^{++}\beta y \sin n^{+}\gamma z\, F_a(x) \\ \sin m^{+}\beta y \sin n^{++}\gamma z\, F_a(x) \\ \sin m^{++}\beta y \sin n^{+}\gamma z\, F_s(x) \end{pmatrix} \right\}$$

$$\mathscr{A}_4 = \mathscr{A}_0 + \left\{ \phi: \begin{pmatrix} \cos m^{+}\beta y \sin n^{++}\gamma z\, F_s(x) \\ \cos m^{++}\beta y \sin n^{+}\gamma z\, F_a(x) \\ \sin m^{+}\beta y \sin n^{++}\gamma z\, F_a(x) \\ \sin m^{++}\beta y \sin n^{+}\gamma z\, F_s(x) \end{pmatrix} \quad \psi: \begin{pmatrix} \cos m^{+}\beta y \cos n^{++}\gamma z\, F_s(x) \\ \cos m^{++}\beta y \cos n^{+}\gamma z\, F_a(x) \\ \sin m^{+}\beta y \cos n^{++}\gamma z\, F_a(x) \\ \sin m^{++}\beta y \cos n^{+}\gamma z\, F_s(x) \end{pmatrix} \right\}$$

$$\mathscr{A}_5 = \mathscr{A}_0 + \left\{ \phi: \begin{pmatrix} \cos m^{+}\beta y \sin n^{+}\gamma z\, F_s(x) \\ \cos m^{++}\beta y \sin n^{++}\gamma z\, F_a(x) \\ \sin m^{+}\beta y \sin n^{+}\gamma z\, F_a(x) \\ \sin m^{++}\beta y \sin n^{++}\gamma z\, F_s(x) \end{pmatrix}, \quad \psi: \begin{pmatrix} \cos m^{+}\beta y \cos n^{+}\gamma z\, F_s(x) \\ \cos m^{++}\beta y \cos n^{++}\gamma z\, F_a(x) \\ \sin m^{+}\beta y \cos n^{+}\gamma z\, F_a(x) \\ \sin m^{++}\beta y \cos n^{++}\gamma z\, F_s(x) \end{pmatrix} \right\}$$

$$\mathscr{A}_6 = \mathscr{A}_0 + \left\{ \phi: \begin{pmatrix} \sin m^{+}\beta y \sin n^{+}\gamma z\, F_s(x) \\ \cos m^{++}\beta y \sin n^{++}\gamma z\, F_s(x) \\ \cos m^{+}\beta y \sin n^{+}\gamma z\, F_a(x) \\ \sin m^{++}\beta y \sin n^{++}\gamma z\, F_a(x) \end{pmatrix}, \quad \psi: \begin{pmatrix} \sin m^{+}\beta y \cos n^{+}\gamma z\, F_s(x) \\ \cos m^{++}\beta y \cos n^{++}\gamma z\, F_s(x) \\ \cos m^{+}\beta y \cos n^{+}\gamma z\, F_a(x) \\ \sin m^{++}\beta y \cos n^{++}\gamma z\, F_a(x) \end{pmatrix} \right\}$$

$$\mathscr{A}_7 = \mathscr{A}_0 + \left\{ \phi : \begin{pmatrix} \sin m^{+}\beta y \cos n^{+}\gamma z\, F_{\mathrm{s}}(x) \\ \cos m^{++}\beta y \cos n^{++}\gamma z\, F_{\mathrm{s}}(x) \\ \cos m^{+}\beta y \cos n^{+}\gamma z\, F_{\mathrm{a}}(x) \\ \sin m^{++}\beta y \cos n^{++}\gamma z\, F_{\mathrm{a}}(x) \end{pmatrix}, \quad \psi : \begin{pmatrix} \sin m^{+}\beta y \sin n^{+}\gamma z\, F_{\mathrm{s}}(x) \\ \cos m^{++}\beta y \sin n^{++}\gamma z\, F_{\mathrm{s}}(x) \\ \cos m^{+}\beta y \sin n^{+}\gamma z\, F_{\mathrm{a}}(x) \\ \sin m^{++}\beta y \sin n^{++}\gamma z\, F_{\mathrm{a}}(x) \end{pmatrix} \right\}$$

It is easy to show that the sets $\mathscr{A}_1$, $\mathscr{A}_2$, $\mathscr{A}_6$ and $\mathscr{A}_7$ include $\mathscr{U}_0$ by setting $m^{++} = 0$. For comparison with $\mathscr{U}_0$ expressed in (27), translate the z-axis by $\pi/2\gamma$ for the set $\mathscr{A}_2$ The subharmonics $\frac{1}{2}\gamma$ must be introduced for the sets $\mathscr{A}_6$ and $\mathscr{A}_7$.

REFERENCES

Andereck, D. D., Dickman, R. & Swinney, H. L. 1983 New flows in a circular Couette system with co-rotating cylinders. *Phys. Fluids* **26**, 1395–1401.

Chandrasekhar, S. 1961 *Hydrodynamic and Hydromagnetic Stability*. Oxford University Press.

Clever, R. M. & Busse, F. H. 1974 Transition to time-dependent convection. *J. Fluid Mech.* **65**, 625–645.

DiPrima, R. C. & Swinney, H. L. 1981 Instabilities and transition in flow between concentric rotating cylinders. In *Hydrodynamic Instabilities and the Transition to Turbulence* (ed. H. L. Swinney & J. P. Gollub), pp. 139–180. Springer.

Drazin, P. G. & Reid, W. H. 1981 *Hydrodynamic Stability*. Cambridge University Press.

Eagles, P. M. 1974 On the torque of wavy vortices. *J. Fluid Mech.* **62**, 1–9.

Jones, C. A. 1981 Nonlinear Taylor vortices and their stability. *J. Fluid Mech.* **102**, 249–261.

Nagata, M. & Busse, F. H. 1983 Three-dimensional tertiary motions in a plane shear layer. *J. Fluid Mech.* **135**, 1–26.

Rayleigh, Lord 1880 On the stability, or instability, of certain fluid motions. *Proc. Lond. Math. Soc.* **11**, 57–70.

Taylor, G. I. 1921 Experiments with rotating fluids. *Proc. Camb. Phil. Soc.* **20**, 326–329.

Taylor, G. I. 1923 Stability of a viscous liquid contained between two rotating cylinders. *Phil. Trans. Roy. Soc. Lond.* A **223**, 289–343.